Cell Reports
Physical Science

CellPress
OPEN ACCESS

Article

Large Dzyaloshinskii-Moriya interaction and room-temperature nanoscale skyrmions in CoFeB/MgO heterostructures

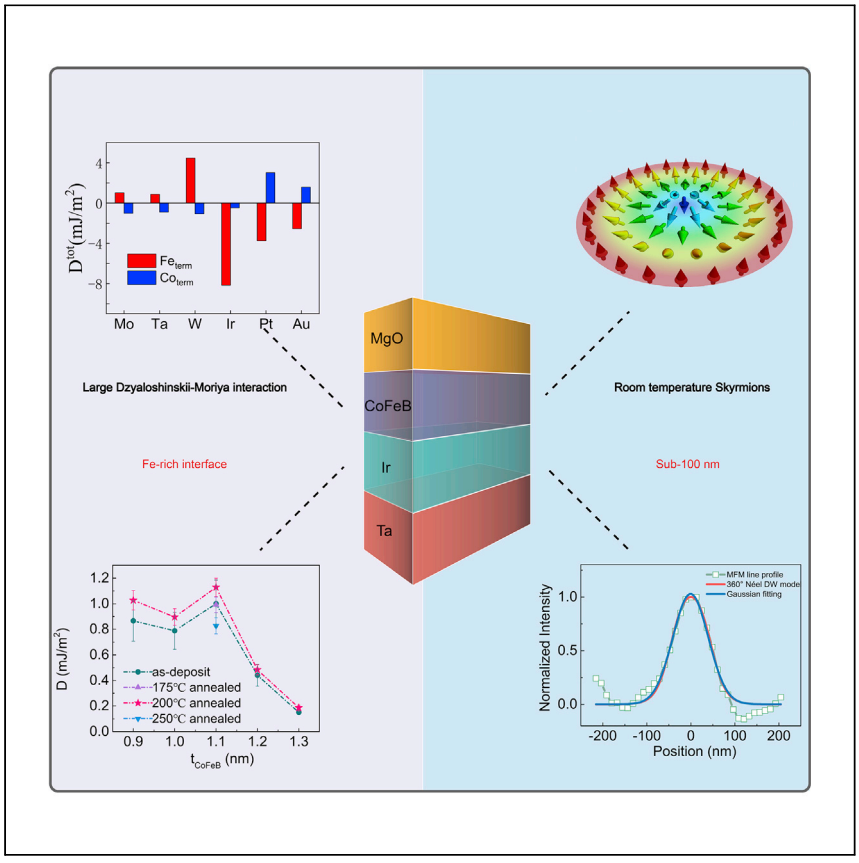

Chen et al. observe a large Dzyaloshinskii-Moriya interaction, combined with the evidence of sub-100-nm room-temperature skyrmions in Ir/CoFeB/MgO structures. This material stack may provide a platform to realize skyrmionics, especially the nucleation and electrical detection of skyrmions in perpendicular anisotropy-based magnetic tunnel junctions.

Runze Chen, Xinran Wang, Houyi Cheng, ..., Shouzhong Peng, Xueying Zhang, Weisheng Zhao

shouzhong.peng@buaa.edu.cn (S.P.)
xueying.zhang@buaa.edu.cn (X.Z.)
weisheng.zhao@buaa.edu.cn (W.Z.)

Highlights

Large DMI in Ir/CoFeB/MgO thin films with perpendicular magnetic anisotropy

First-principles calculations combined with Brillouin light-scattering methods

Significant role of interfacial configuration on the regulation of DMI

Sub-100 nm room-temperature magnetic skyrmions in Ir/CoFeB/MgO multilayers

Chen et al., Cell Reports Physical Science 2, 100618
November 17, 2021
https://doi.org/10.1016/j.xcrp.2021.100618

Cell Reports
Physical Science

CellPress
OPEN ACCESS

Article

Large Dzyaloshinskii-Moriya interaction and room-temperature nanoscale skyrmions in CoFeB/MgO heterostructures

Runze Chen,[1,6] Xinran Wang,[1,2,6] Houyi Cheng,[1,3,6] Kyu-Joon Lee,[4] Danrong Xiong,[1] Jun-Young Kim,[4] Sai Li,[1] Hongxin Yang,[5] Hongchao Zhang,[1,2] Kaihua Cao,[1,2] Mathias Kläui,[4] Shouzhong Peng,[1,3,*] Xueying Zhang,[1,2,*] and Weisheng Zhao[1,2,3,7,*]

SUMMARY

Magnetic skyrmions in heavy metal (HM)/CoFeB/MgO structures are of particular interest for skyrmion-based magnetic tunnel junction (MTJ) devices because of their reliable generation, stability, and readout through purely electrical methods. To optimize the properties, such as stability, a strong Dzyaloshinskii-Moriya interaction (DMI) is required at room temperature. Here, using first-principles calculations, we demonstrate that huge DMI can be obtained in Ir/CoFe structures with an Fe-terminated configuration. Moreover, Brillouin light-scattering measurements show that indeed Ta/Ir/$Co_{20}Fe_{60}B_{20}$/MgO thin films with perpendicular magnetic anisotropy exhibit a large DMI value (1.13 mJ/m^2) when the thickness of the CoFeB layer is 1.1 nm, which can be attributed to the smooth and Fe-rich interface between Ir and CoFeB layers. Furthermore, we observe stable sub-100 nm magnetic skyrmions at room temperature in the Ir/CoFeB/MgO systems by magnetic force microscope. This work paves the way for promoting the application of skyrmions in CoFeB/MgO-based perpendicular anisotropy MTJ structures.

INTRODUCTION

The Dzyaloshinskii-Moriya interaction (DMI) is an antisymmetric exchange interaction that originates from the presence of the spin-orbit coupling (SOC) combined with a structure inversion asymmetry.[1–3] It plays a crucial role in the formation and stabilization of topological magnetic textures, such as chiral domain walls[4] and magnetic skyrmions.[5,6] These chiral magnetic structures are promising for use as information carriers in novel memory-storage and neuromorphic computing devices thanks to their small size and current-driven motion at low current densities.[7,8] The DMI can be induced at heavy metal (HM)/ferromagnetic metal (FM) structures due to the strong SOC of the heavy element.[9,10] In these structures, such as Pt/Co/Ta,[11] Ir/Fe/Co/Pt,[12] and Pt/Co/MgO,[13] magnetic skyrmions can be stabilized at room temperature, where the skyrmion size, density, and stability exhibit strong dependence on interfacial DMI.

However, the controllable nucleation and detection of skyrmions through purely electrical means are still difficult issues, hindering the application of skyrmion-based devices. To address these concerns, combining skyrmions with perpendicular anisotropy-based magnetic tunnel junctions (p-MTJs), using the tunnel magnetoresistance ratio (TMR) for the electrical detection of skyrmions is one of the possible

[1]Fert Beijing Institute, School of Integrated Circuit Science and Engineering, Beijing Advanced Innovation Center for Big Data and Brain Computing, Beihang University, Beijing 100191, China

[2]Beihang-Goertek Joint Microelectronics Institute, Qingdao Research Institute, Beihang University, Qingdao 266000, China

[3]Hefei Innovation Research Institute, Beihang University, Hefei 230013, China

[4]Institute of Physics, Johannes Gutenberg University Mainz, 55099 Mainz, Germany

[5]Ningbo Institute of Materials Technology and Engineering, Chinese Academy of Sciences, Ningbo 315201, China

[6]These authors contributed equally

[7]Lead contact

*Correspondence: shouzhong.peng@buaa.edu.cn (S.P.), xueying.zhang@buaa.edu.cn (X.Z.), weisheng.zhao@buaa.edu.cn (W.Z.)

https://doi.org/10.1016/j.xcrp.2021.100618

solutions.[14–16] TMR is sensitive to the magnetization of an MTJ's constituent magnetic layers, and the TMR detection method used in MTJs is compatible with current CMOS technology, promising the industrial integration.[17] To meet the challenge of practical skyrmions detection using MTJs, it is prerequisite to engineer magnetic structure necessary to induce skyrmionic state and be applied in MTJs. Thus, HM/CoFeB/MgO structures, which have already demonstrated high TMR in CoFeB/MgO-based p-MTJs,[18,19] become a promising skyrmion-hosting material stack. In experiments, room-temperature skyrmions have been generated by current pulses in Pt/CoFeB/MgO structures;[20] meanwhile, some theoretical studies have suggested the practicality of HM/CoFeB/MgO-based MTJ for the skyrmionic state detection.[21,22] On the other hand, the strong DMI is beneficial for the stability of skyrmions, which is helpful for the manipulation of skyrmions at room termperature. Thus, a sufficiently large DMI in HM/CoFeB/MgO ultra-thin films is needed and the underlying physical mechanisms of the DMI in these structures also need to be revealed.

In this paper, using first-principles calculations, we evaluate and analyze the DMI behavior in HM/CoFe structures. We demonstrate that in addition to HM elements, the DMI is sensitive to the interfacial configurations. More importantly, Ir/CoFe structures with Fe-terminated configuration are predicted to exhibit the strongest DMI among all the HM/CoFe structures. We attribute the variation of DMI between two interfacial configurations of Ir/CoFe structures to the different spin mixing 5*d* orbital transitions of interfacial Ir atoms. Moreover, we experimentally investigate the DMI in Ta/Ir/$Co_{20}Fe_{60}B_{20}$/MgO thin films by Brillouin light-scattering (BLS) measurements, and a considerably strong DMI up to 1.13 mJ/m^2 when the thickness of CoFeB layer is 1.1 nm is observed. Furthermore, sub-100-nm–magnetic skyrmions in Ir/CoFeB/MgO stacks are detected using magnetic force microscopy (MFM) at room temperature. Our findings would further help control DMI and thus manipulate the magnetic skyrmions in CoFeB/MgO heterostructures, paving way for integration and application of the skyrmion-based devices.

RESULTS AND DISCUSSION

First-principles calculations

To theoretically investigate the DMI of HM/CoFe structures, we perform density functional theory (DFT) calculations of the DMI energy for the X/CoFe (X = Mo, Ta, W, Ir, Pt, and Au) structures. These X metals are commonly used in MTJ process, which have been found to have various excellent properties in different experiments.[18,19,23–25] It is worth mentioning that previous experimental studies[26,27] demonstrated a low contribution to the DMI from the CoFeB/MgO interface in HM/CoFeB/MgO structures. Hence, we focus on the DMI of the HM/CoFe structures here. Considering that both Fe and Co atoms exist at the HM/CoFeB interface in experiments, Fe-terminated and Co-terminated configurations are adopted in our calculations. The crystalline structures of X/CoFe are shown in Figures 1A and 1B (only the Co-terminated structures are shown here), where five-monolayers of a body-centered cubic (bcc) CoFe(001) film is located on the three-monolayers face-centered cubic (fcc) X(001) film. Arrows schematically indicate the X/CoFe structures with clockwise (CW) (left panel) and anticlockwise (CCW) (right panel) spin-spiral chirality.

We use constrained spin-spiral supercell approach to calculate the microscopic DMI strength d^{tot} and micromagnetic DMI coefficient D^{tot}.[28,29] In our calculations, a positive DMI representing CCW (left-handed) chirality and a negative DMI

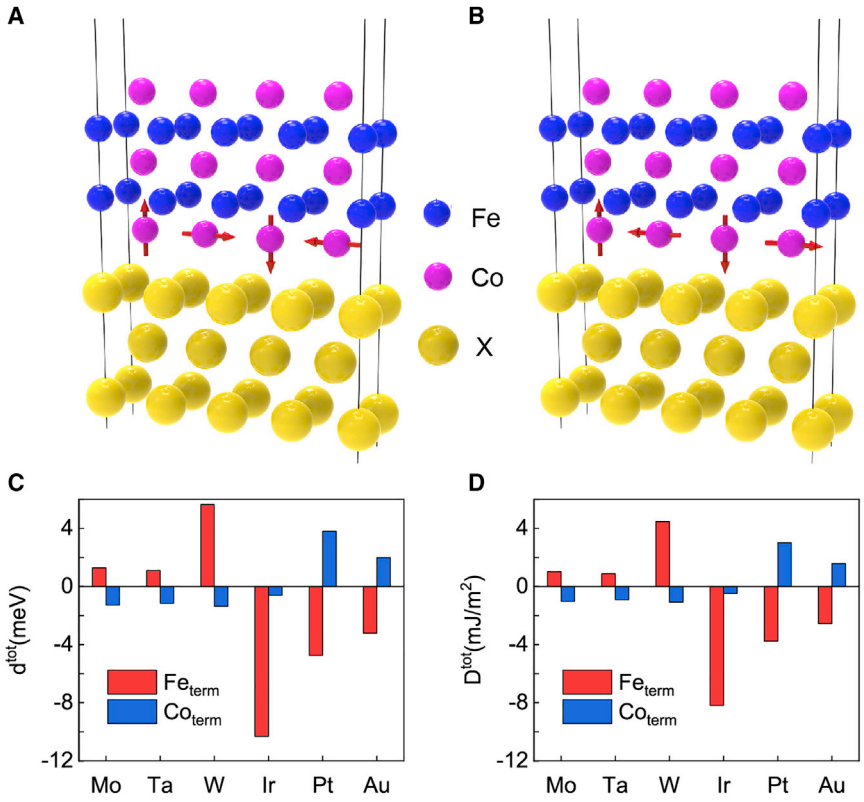

Figure 1. Crystal and spin configurations of X/CoFe structures and the calculated total DMI energy

(A and B) Schematic of the ideal array of atoms of X/CoFe (X = Mo, Ta, W, Ir, Pt, and Au) structures used for DMI calculations. Blue, purple and yellow balls represent iron, cobalt and X atoms, respectively. The DMI is calculated as the energy difference of the clockwise and counterclockwise spin configurations, as schematically by arrows (Only the Co-terminated structure is shown here). (C and D) The calculated total DMI strength d^{tot} and the corresponding micromagnetic DMI coefficient D^{tot} of different structures with two interface configurations. The DMI values change significantly with different HM elements and with two interfacial configurations. Especially for Ir/CoFe structures, this discrepancy is particularly large. The DMI magnitude of Ir/CoFe structure with Fe-terminated configuration is the largest one among all the X/CoFe structures in our calculations.

representing CW (right-handed) chirality is adopted. Figures 1C and 1D shows the calculated total DMI strength d^{tot} and the corresponding micromagnetic DMI coefficient D^{tot} of X/CoFe structures with two different interfacial configurations. One can see that the DMI values change significantly with different HM elements, which has been confirmed by many experimental and theoretical studies.[26,30,31] More importantly, in all structures the DMI varies between two interfacial configurations. Especially for Ir/CoFe structures, this discrepancy is particularly significant. The DMI strength for the Co-terminated Ir/CoFe is negligible (−0.6 meV), but it increases dramatically to −10.3 meV for the Fe-terminated one. In particular, this Ir/CoFe structure with Fe-terminated configuration possesses the largest DMI magnitude among all the HM/CoFe structures in our calculations. The great difference of DMI magnitude between the two types of interfacial configurations implies the considerable controllability of DMI through interface engineering in the Ir/CoFe structures. Specifically, by comparing the binding energy of Ir/CoFe structures between two interfacial configurations, the Fe-terminated case is found to be the most energetically preferable structure (See Note S1 and Table S1), indicating that the Ir/CoFeB/

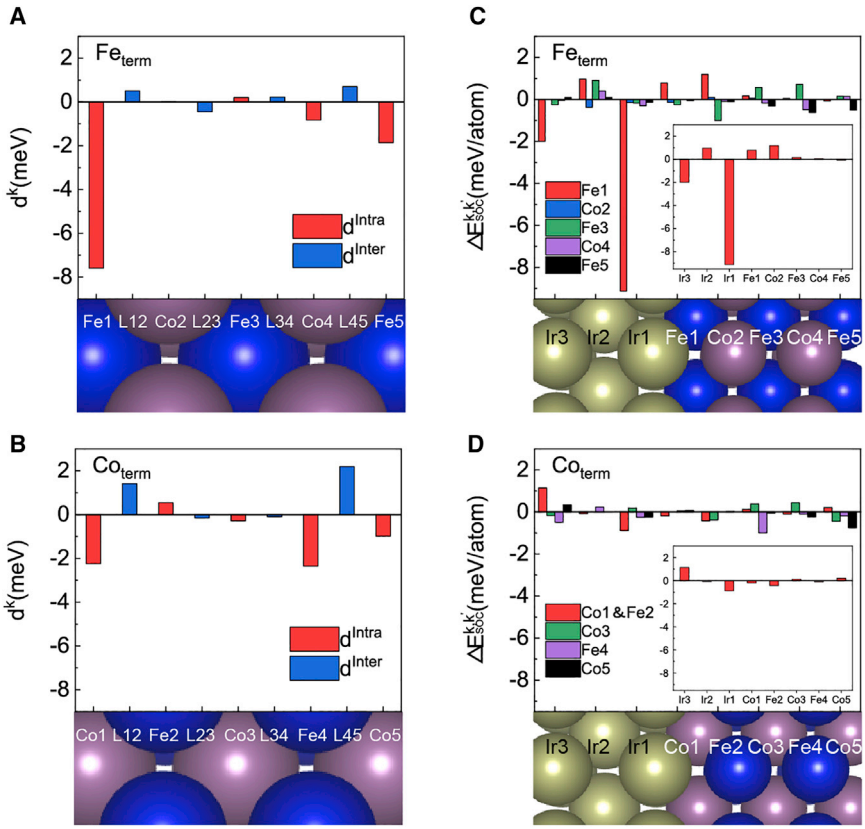

Figure 2. Anatomy of DMI for Ir/CoFe bilayers

(A and B) Layer-resolved DMI strength d^k of corresponding layer k for the Fe-terminated and the Co-terminated configurations of Ir/CoFe structures. L12, L23, L34, and L45 represent the interlayer between two adjacent magnetic layers and the corresponding d^{L12}, d^{L23}, d^{L34}, and d^{L45} represent the interlayer contribution of DMI. For Fe-terminated configuration, the DMI is predominantly located at the first Fe layer, providing large negative contribution to the total DMI. For Co-terminated configuration, the interlayer L12 provides a non-negligible contribution with the inverse sign of the contribution from the first Co layer, resulting in very small overall DMI.

(C and D) Corresponding SOC energy distribution in the atomic sites of all layers k' for the two configurations of Ir/CoFe structures. For clarity, the distributions of SOC energy variations induced by the interfacial magnetic layers are shown (inset). The most obvious feature is that the SOC energy source in both configurations is predominantly located at the interfacial Ir1 layer.

MgO structures have an enormous potential to reach a large DMI value in case of Fe-rich interface, which is corroborated by the following experiments.

The origin of the DMI variation with different HM elements and interfacial configurations can be understood from the analysis of layer-resolved DMI and associated SOC energy distribution for X/CoFe structures. In particular, the results for layer-resolved DMI of Ir/CoFe structures with Fe-terminated and Co-terminated configurations are shown in Figure 2A and 2B, respectively. The x-coordinate represents the different magnetic layers k, and the DMI strength for each magnetic layer is expressed as d^k. It is worth noting that L12 in our calculations represents the interlayer between the first and second magnetic layers and the corresponding d^{L12} represents the interlayer contribution of DMI. The similar definition is also given on d^{L23}, d^{L34}, and d^{L45}. One can see that in both configurations the DMI is concentrated on the interfacial magnetic layers. For Fe-terminated case, the DMI is predominantly located at the first Fe layer, providing large negative contribution to the total

DMI, as indicated by the red bar of Fe1 in Figure 2A. However, in the case of Co-terminated configuration, the DMI is not only located at the first magnetic layer, the second layer and the interlayer between the first and second magnetic layers also make contributions to the total DMI. As illustrated by the red bar of Co1 and the blue bar of L12 in Figure 2B, the interlayer provides a non-negligible contribution counteracting that of the first Co layer, resulting in a very weak overall DMI.

To clear up the origin of the considerable difference in interfacial DMI between two configurations of Ir/CoFe structures, layer-resolved SOC energy distributions is calculated. Figures 2C and 2D present the results of SOC energy distribution corresponding to the layer-resolved DMI for the two configurations. $\triangle E_{SOC}^{k,\,k'}$ represents the SOC energy difference in the atomic layer k' between spin configurations of opposite chirality in the magnetic layer k. We use Co1&Fe2 to represent the first two magnetic layers that will contribute to the DMI for Co-terminated configuration. In this case, the corresponding $\triangle E_{SOC}^{Co1\,\&\,Fe2,\,k'}$ can be defined as the SOC energy difference in the atomic layer k' associated with the DMI strength of the interfacial magnetic layers (Co1, Fe2, and the interlayer between Co1 and Fe2). For clarity, the distributions of SOC energy variations induced by the interfacial magnetic layers (Fe1 for Fe-terminated case, Co1&Fe2 for Co-terminated case) are shown in the inset of Figures 2C and 2D. The most obvious feature is that the SOC energy source in both configurations is predominantly located at the interfacial Ir1 layer. For the Fe-terminated configuration, the strong DMI between the interfacial Fe spins (Fe1) is associated with a large SOC energy source $\triangle E_{SOC}^{Fe1,\,Ir1}$ in the adjacent Ir layer. At the same time, the SOC energy source $\triangle E_{SOC}^{Co1\&Fe2,\,Ir1}$ located at the interfacial Ir layer for the case of Co-terminated configuration is extremely small, indicating a negligible DMI at Ir/CoFe interface. Therefore, the enormous discrepancy in interfacial DMI of the two configurations of Ir/CoFe structures originates from the huge variation of the SOC energy in the interfacial Ir layers, due to the different combinations of Ir and magnetic atoms at the interface (Ir-Fe or Ir-Co). Here, we also calculate the layer-resolved SOC energy distribution when considering the DMI contribution from the first two magnetic layers for Fe-terminated configuration. It can be seen that the SOC energy source in the interfacial Ir layer is almost unchanged when we consider the first two magnetic layers, which further indicates that the DMI strength is concentrated on the first magnetic layer Fe1 for the Ir/CoFe structure with Fe-terminated configuration (See Note S2 and Figure S1).

The same conclusion can be drawn for other X/CoFe structures. Through the calculations of layer-resolved DMI and the corresponding localization of SOC energy for other X/CoFe structures with two interfacial configurations, we also find that the interfacial DMI comes from the SOC energy source of HM atoms at the interface. It is the difference of SOC energy source in different structures that leads to the significant difference of DMI (See Note S3 and Figures S2–S6). By comparing the results of Ir/CoFe structures with other X/CoFe structures, we can conclude that the largest SOC energy source for the interfacial Ir layer of Ir/CoFe structure with the Fe-terminated configuration results in the strongest DMI among all the structures, which shows that we can get a considerable DMI in Ir/CoFeB/MgO structure with an Fe-rich interface.

The mechanism of DMI variation with 5*d* HM atoms has been widely studied, where the chemical trend of DMI depends on interfacial hybridization between relevant *d* orbitals of the 3*d* and 5*d* atoms and on orbital contributions of the 5*d* heavy elements.[31,32] However, a deeper understanding of the impact of interfacial

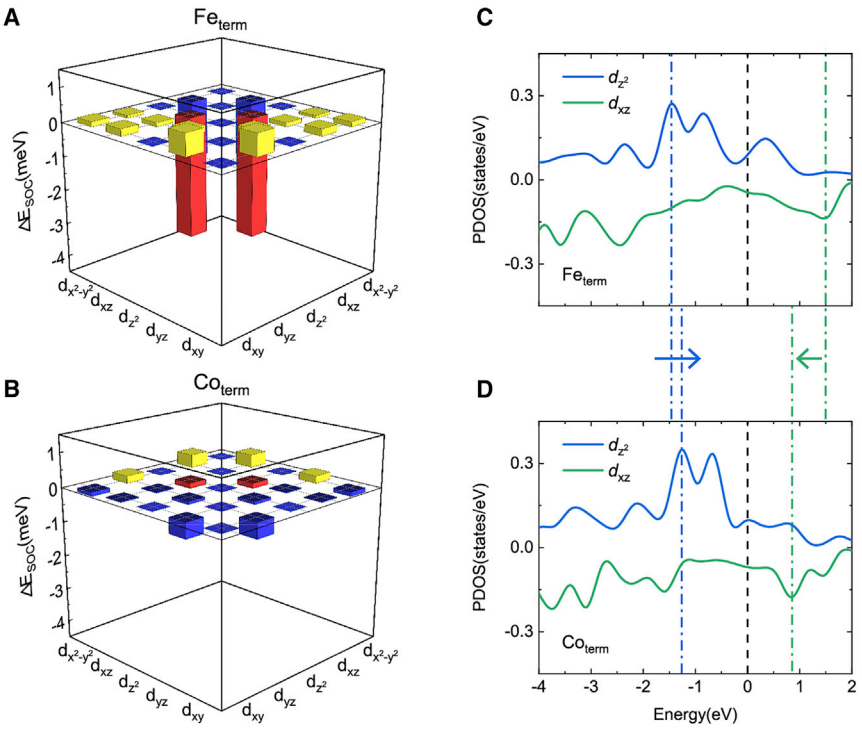

Figure 3. Orbital resolved SOC energy and projected density of states

(A and B) 5*d* Orbital-resolved SOC energy of the interfacial Ir atoms in Fe-terminated and Co-terminated structures. Red bars represent the largest discrepancy between the two structures comes from the SOC matrix element corresponding to the transition between d_{z^2} and d_{xz} orbitals. (C and D) Projected density of states (PDOSs) of interfacial Ir atoms for the Fe-terminated and Co-terminated structures, only majority d_{z^2} and minority d_{xz}states of the 5*d* orbitals are considered. blue and green arrows represent the energy shift of majority d_{z^2} and minorityd_{xz}states from Fe-terminated configuration to Co-terminated configuration, respectively. The shift of energy levels of corresponding electronic orbitals between two configurations results in the change of the occupation of their electronic states, and ultimately in DMI.

configurations on DMI is still lacking. Next, only the Ir/CoFe structures are analyzed to elucidate this mechanism. In the case of Ir/CoFe structures with Fe-terminated and Co-terminated configurations, the hybridization between *d* orbitals of the magnetic and nonmagnetic sites exhibit similar contributions to DMI due to the similar topologies of band structures.[31] Consequently, it is the variation of 5*d* orbital contributions of interfacial Ir atoms, more specifically, 5*d* orbital SOC spin mixing transition terms, that makes the DMI quite different between the two interfacial configurations.[32–34] Figures 2C and 2D show the significant difference in SOC energy of the interfacial Ir layer between two interfacial configurations, resulting in great difference in interfacial DMI. To further elucidate the origin of the discrepancy in SOC energy, we calculate the 5*d* orbital-resolved SOC energy of interfacial Ir atoms in both cases as shown in Figures 3A and 3B. It can be seen that the largest discrepancy between the two structures comes from the SOC matrix element corresponding to the transition between d_{z^2} and d_{xz} orbitals (red bar), which is strongly negative for Fe-terminated configuration but negligible for Co-terminated case.

To better analyze the influence of transitions between d_{z^2} and d_{xz} orbitals of the interfacial Ir atoms on DMI, we employ the analysis based on the first-order perturbation theory. According to the first-order perturbation expression of the corrected total energy

due to DMI, the occupied states comprising different 5*d* orbitals and spins of the interfacial Ir atoms provide the major contribution to DMI, which can be denoted in the form of expectation value $<\psi_{lm,s}|\hat{H}_{soc}|\psi_{lm,s}>$, where $\hat{H}_{soc}$ is the SOC operator, and $|\psi_{lm,s}>$ denotes the spin-dependent occupied states of interfacial Ir atoms.[35] As shown by our calculations of the 5*d* orbital-resolved SOC energy, the SOC matrix elements between d_{z^2} and d_{xz} orbitals of the two structures are negative and vary the most. Meanwhile, following the theoretical analysis of the spin mixing transition terms between 5*d* orbitals, we can find that the expectation value of $<d_{z^2}\chi_+ + d_{xz}\chi_-|\hat{H}_{soc}|d_{z^2}\chi_+ + d_{xz}\chi_->$ is negative and has the largest absolute value among all the spin mixing terms.[33] Therefore, combined with the calculations of 5*d* orbital-resolved SOC energy of interfacial Ir atoms mentioned above, the expectation value of $<d_{z^2}\chi_+ + d_{xz}\chi_-|\hat{H}_{soc}|d_{z^2}\chi_+ + d_{xz}\chi_->$ mainly contributes to the discrepancy of DMI between two interfacial configurations for Ir/CoFe structures. In Figures 3C and 3D, we show the projected density of states (PDOS) of interfacial Ir atoms for the Fe-terminated and the Co-terminated structures. For clarity, we only consider the majority d_{z^2} states and the minority d_{xz} states of the 5*d* orbitals. The obvious variation of PDOS from the Fe-terminated configuration to the Co-terminated configuration is that the majority d_{z^2} states $(d_{z^2}\chi_+)$ shift upward in energy level associated with a decrease of their occupation (blue arrow) and the minority d_{xz} states $(d_{xz}\chi_-)$ shift downward in energy level corresponding to an increase of their occupation (green arrow). Consider the correction term $<d_{z^2}\chi_+ + d_{xz}\chi_-|\hat{H}_{soc}|d_{z^2}\chi_+ + d_{xz}\chi_->$, since the decreasing extent of $d_{z^2}\chi_+$ is higher than the increasing extent of $d_{xz}\chi_-$[33], this correction matrix element decreases in magnitude from the Fe-terminated structure to the Co-terminated structure, which causes a large DMI strength for Fe-terminated case but a much smaller DMI for Co-terminated case. To sum up, the different spin mixing transitions between d_{z^2} and d_{xz} orbitals of interfacial Ir atoms for the two configurations shifts the energy levels of corresponding electronic orbitals, resulting in a change in the occupation of their electronic states, and ultimately in the DMI.

Characterization of the DMI by BLS experiments

In order to probe the existence of large DMI in Ir/CoFe structures, a series of experiments were carried out. The samples of Sub/Ta(5)/Ir(5)/$Co_{20}Fe_{60}B_{20}$(*t*)/MgO(2)/Ta(3) are deposited on the thermally oxidized Si wafers at room temperature and without applying magnetic fields, as shown in Figure 4A. The numbers in parentheses represent the thickness of each layer in nanometers, *t* is the thickness of the CoFeB layer ranging from 0.9 nm to 1.3 nm. We choose the Fe-rich CoFeB target, in which the proportion of Co, Fe, and B is 20%, 60%, and 20%, respectively. The bottom Ta layer is the buffer layer to improve the quality of the interface between Ir and CoFeB layers, and the top Ta layer prevents the film from air-passivation. Figure 4B shows the high-resolution transmission electron microscopy (HR-TEM) images and energy-dispersive X-ray spectroscopy (EDX) line of the as-deposited sample with the CoFeB thickness of 1.1 nm. The individual-element slices of a selected region of the HR-TEM image are shown in Figure 4C. The good interfacial uniformity and sharp interface can be seen in the HR-TEM images, showing the high-quality of the thin films. From the EDX images we can also know that the atom of B is attracted by Ir layer, which makes the crystalline property of CoFe layer better and improves the quality of the films after annealing[36] (See Note S5). The EDX line shows the presence of both Fe and Co atoms at the interface between Ir and CoFeB layers, but the content of Fe is higher than that of Co, as evidenced in the micro-area analysis image, which is consistent with the elements proportion of the $Co_{20}Fe_{60}B_{20}$ target we used. (See Note S4 and Figure S7).

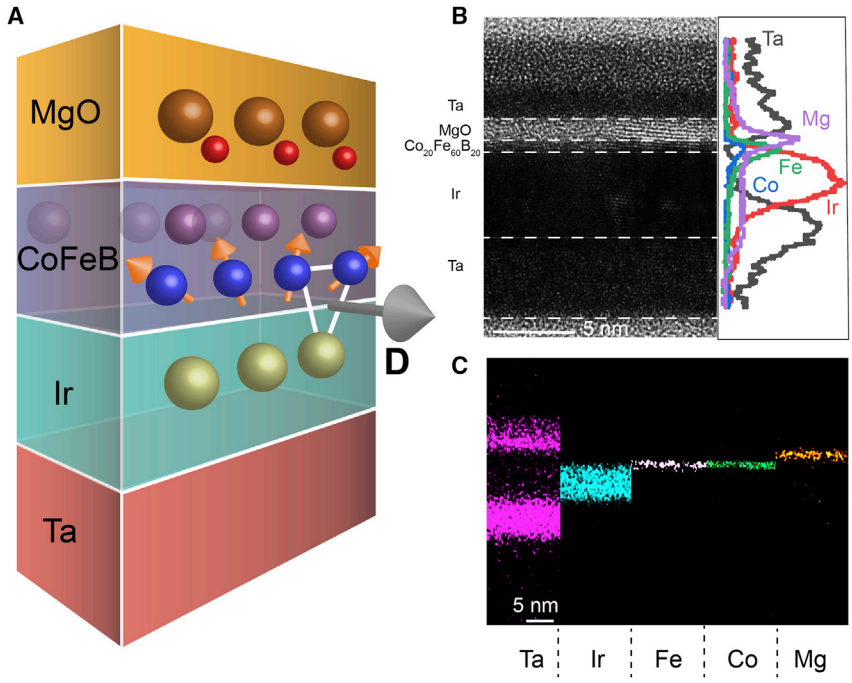

Figure 4. Film configuration and characterization

(A) Schematic of the Ta/Ir/CoFeB/MgO stack structure. The bottom Ta layer is the buffer layer to improve the quality of the interface between Ir and CoFeB layers. Large DMI vector *D* can be induced at Ir/CoFeB interface.

(B) The corresponding high-resolution transmission electron microscopy (HR-TEM) image and energy-dispersive X-ray spectroscopy (EDX) line profiles of the as-deposited Ta/Ir/CoFeB/MgO sample with CoFeB thickness of 1.1 nm. From the figure, we can see that the sharp interface and good crystallinity, which indicates that the film has good quality. At the same time, the proportion of Fe atoms in Ir/CoFeB interface is larger than that of Co atoms, which demonstrates that the current Fe-rich interface.

(C) The individual-element slices of a selected region of the HR-TEM image in (B). The results confirm our depositional sequence and indicate that the degree of diffusion is weak under current conditions.

The *M-H* curves (*M* versus magnetic field *H*) are obtained using a vibrating sample magnetometer (VSM). As shown in Figure 5A, all the samples with different CoFeB thicknesses exhibit perpendicular magnetic anisotropy (PMA). To estimate the DMI value, we perform BLS measurements to investigate the asymmetric spin-wave dispersion induced by DMI.[37] The schematic setup is shown in the inset of Figure 5B, where the sample is in-plane magnetized by an external field to realize the Damon–Eshbach (DE) tandem mode,[38] and an incident laser beam with a wavelength of 532 nm is focused on the sample surface. Because of the momentum and energy conservation in the scattering process, the creation (annihilation) of a magnon corresponds to the Stokes (Anti-Stokes) process[39] with the wave-vector $|k| = 4\pi sin\theta/\lambda$,[26,40] where λ is the wavelength of the incident light, θ is the angle of incidence.

Figure 5B shows a normalized BLS spectrum for the as-deposited Ir/CoFeB (1.1 nm)/MgO sample for wave vector k = 21.40 um^{-1} and under an applied field of 1.04 T (Typical spectra for samples of other thickness are shown in Note S8 and Figure S13), from where the Stokes and Anti-Stokes peaks can be determined by Lorenz function fitting. Therefore, the frequency difference $\Delta f = f_s - f_{as}$ due to the presence of DMI

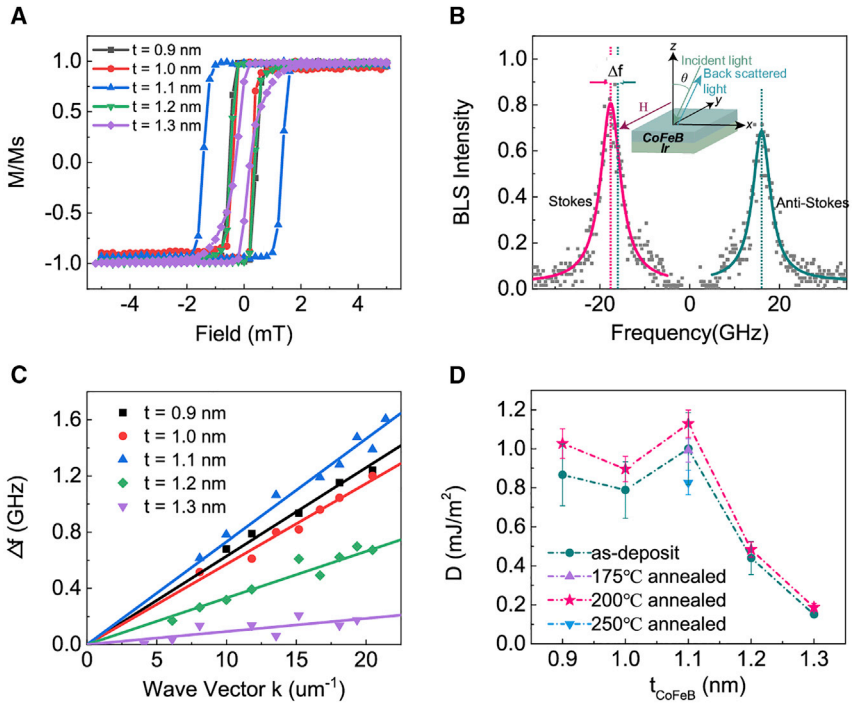

Figure 5. Characterization of the DMI value by BLS measurements

(A) The hysteresis loops with out-of-plane (OP) field for different thicknesses of the CoFeB layer, from where saturated magnetization can be extracted. From the *M-H* curve, it can be seen that the films exhibit perpendicular magnetic anisotropy under different CoFeB thickness. Meanwhile, the value of *Hc* increases first and then decreases with the increase of CoFeB thickness, and *Hc* values reaches the maximum when the CoFeB thickness is 1.1 nm.

(B) Normalized BLS spectra measured for Ir/CoFeB (1.1 nm)/MgO, where the wave vector is $k = 21.40\ um^{-1}$. The inset shows the schematic setup of BLS measurements, where *H* is an in-plane magnetic field of 1.04 T and θ is the incident angle. Symbols refer to the experimental data, whereas the green (red) solid lines are the Lorentzian fitting of Stokes (Anti-Stokes) peak, where a frequency difference Δf can be seen.

(C) The wave vector *k* dependence of the frequency difference Δf in Ir/CoFeB/MgO samples with different thickness. The solid lines are the linear fittings for equation $\Delta f = \frac{2\gamma}{\pi M_s} Dk$ to deduce *D* value.

(D) The DMI constant *D* determined for Ir/CoFeB samples with different CoFeB thickness and at different annealing temperatures. 200°C annealing process strengthens DMI and an optimal value around 1.13 mJ/m^2 is obtained. The error bars take both the fitting errors of Δf-k and Ms into considerations.

could be deduced. The relation between this frequency shift of the counter-propagating spin-waves and the micromagnetic DMI coefficient *D* could be described as $\Delta f = \frac{2\gamma}{\pi M_s} Dk$, where γ is the gyromagnetic ratio, M_s is the saturated magnetization and *k* is the amplitude of wave vector. Contrary to the calculations, in our experiments, positive DMI represents CW (right-handed) chirality.

A linear variation of Δf with the wave vector for different CoFeB thickness is presented in Figure 5C, where the DMI values are extracted from the slopes using the equation mentioned above. Considering $\gamma = 176\ \mathrm{GHz/T}$[26,27,41] and $M_s = 1.54 \times 10^6$ A/m extracted from VSM measurement (Note S6 and Figure S11), we obtain the corresponding thickness dependence curve of the DMI values as shown in Figure 5D. The magnetization *M* can be extracted from the *M-H* curve, after the saturation magnetization M_s and magnetic dead layer t_{DL} can be obtained from

Table 1. Dzyaloshinskii-Moriya interaction (DMI) values in HM/CoFeB systems, determined by BLS measurements

Multilayers	|D| from literature ($mJ\ m^{-2}$)
Ta/CoFeB(1)/MgO	0.036–0.054[26,27]
Ta/CoFeB(0.85–3)/TaOx	0.08–0.22[43,44]
W/CoFeB(0.6–1.5)/MgO	0.073–0.88[26,41,45]
W/CoFeB(0.85)/SiO2	0.25[46]
CoFeB(2)/Pt/Cu	0-0.45[47]
Pt/CoFeB(0.8–1)/MgO	0.8-1[26,48,49]
Pt/CoFeB(1–3)/AlOx	0.58-0.86[10,50]
Pt/CoFeB(2)/Ta	0.51[51]
Pt/CoFeB(1.12)/Ru	0.84[52]
Pt/Ru/CoFeB(1.12)/MgO	0.3[52]
Au/CoFeB(1)/MgO	0.158[26]
IrMn/CoFeB(2)/MgO	0.134[40]
Ir/CoFeB(1)/MgO	0.212[26]
Ir/CoFeB(1.1)/MgO	1.13[a]

Numbers in parentheses represent the thickness of magnetic layer in nanometers.
[a]Represents the result from our experiments

the M/A-t_{CoFeB} curves, where A is the area of the sample and t_{CoFeB} is the thickness of CoFeB layer. M_s is the slope of the curve and the intercept is the value of t_{DL} (See Note S6 for more details). Other than the decrease of DMI strength with the increasing magnetic layer thickness, our DMI constant D displays a slight decline at $t_{CoFeB} < 1.1$ nm and reaches an optimal value around 1.00 ± 0.18 mJ/m^2 at $t_{CoFeB} = 1.1$ nm. When the magnetic layer is relatively thin ($t_{CoFeB} = 0.9, 1.0$ nm), the interdiffusion of Ir and CoFeB at the interface leads to worse interface quality,[42] which is detrimental for the DMI (Corresponding relation between D and t_{CoFeB}^{-1}could be found in Note S7 and Figure S12).

In order to improve the DMI value in our system, we carry out the annealing process for half an hour at 200°C under an out-of-plane field of 1 T for samples of all thickness. The films can still maintain high film quality, strong PMA; and M_s is enhanced to 1.64×10^6 A/m. (See Note S5 and Figures S8–S10, Note S6 and Figure S11). As shown in Figure 5D, after annealing at 200°C, it is clear that for all samples the DMI has been increased. When the thickness of CoFeB layer is 1.1 nm, the DMI value is enhanced up to 1.13 ± 0.07 mJ/m^2, which is a considerably large value for similar CoFeB multilayer systems (Corresponding results of DMI measurements could be found in Note S8 and Figure S14). As demonstrated in many theoretical and experimental studies, the variation of the HM underlayer leads to a significant modification of DMI energy. Table 1 shows the reported DMI values extracted from BLS measurements experiments in different HM/CoFeB (HM = Ta, W, Pt, Au, Ru, Ir, and IrMn) systems (Corresponding comparison of surface DMI could be found in Note S9 and Table S2). Compared with these results, our measured DMI strength in the Ir/CoFeB system is much higher, which agrees with the results of our first-principles calculations.

Thermal annealing is widely used in semiconductor process to produce a crystallized MgO tunnel barrier, leading to enhanced MR. Our previous work[53] has found that thermal annealing plays an effect on DMI. Therefore, it is important to investigate how the DMI changes with the annealing temperature. The sample with 1.1 nm CoFeB is annealed at different temperatures (See BLS measurement details in Note S8 and Figure S15). As shown in Figure 5D, it can be clearly seen that D remains almost

Table 2. Dzyaloshinskii-Moriya interaction (DMI) values for comparisons of buffer layer and interfacial configurations

	Multilayers	CoFeB thickness (nm)	|D| from our measurement ($mJ\ m^{-2}$)
Buffer layer	Ta/Ir/CoFeB/MgO	0.9nm	0.86 ± 0.16
	Ir/CoFeB/MgO	0.9nm	0.37 ± 0.03
	Ta/Ir/CoFeB/MgO	1.0nm	0.79 ± 0.15
	Ir/CoFeB/MgO	1.0nm	0.31 ± 0.02
Interfacial Configurations	Ta/Ir/CoFeB/MgO (Fe-rich interface)	1.1nm	1.00 ± 0.18
	Ta/Ir/CoFeB/MgO (Co-rich interface)	1.1nm	0.15 ± 0.03

Comparative experiments are based on the as-deposited Substrate/Ta(5)/Ir(5)/$CCo_{20}FFe_{60}B_{20}$/ MgO(2)/ Ta(3) structures

unchanged at 175°C, and then increases as the temperature rises to 200°C, reaching the maximum value of 1.13 ± 0.07 mJ/m^2, implying that annealing at 200°C can improve the interface quality between Ir and CoFeB layers. However, due to the activity of Ir and the diffusion of B atoms, when the annealing temperature is increased to 250°C, the quality of the Ir/CoFe interface is deteriorating, causing a significant decrease in DMI. As shown in the HR-TEM images, by depositing the buffer Ta layer, the interface quality of the films enhanced, which can explain why Ta as a buffer layer can increase DMI (See Note S5 for more details). Therefore, how to make this system withstand higher temperature while ensuring the interfacial quality to achieve higher DMI is worth further exploration.

Next, our DMI values are larger than previous observation in similar Ir/CoFeB/MgO systems.[26] It is owing to the good Ir/CoFeB interface uniformity and film crystallization induced by the addition of Ta buffer layer,[54,55] and this good interface quality has been demonstrated by the HR-TEM images above. To verify this, samples with t_{CoFeB} = 0.9 nm and 1.0 nm without Ta buffer layer are prepared, and the measurement results are shown in Table 2 (For details see Note S10 and Figure S16). Without Ta used as buffer layer, for both CoFeB thickness, *D* is reduced by about 60%, which is consistent with the previous report,[26] demonstrating the contribution of the buffer layer Ta to the improvement of DMI.

To further probe the influence of interfacial configurations on DMI, as suggested by our calculations, we deposit a small amount of Co at the interface between Ir and CoFeB layers in the sample of Ta/Ir/$Co_{20}Fe_{60}B_{20}$/MgO to form a Co-rich interface. It is worth noting that the small amount of Co cannot form an entire atomic layer, but only increases the proportion of Co atoms at Ir/CoFe interface, that is, the addition of Co elements will not increase the thickness of FM layer and the thickness is maintained at 1.1 nm. Compared with the original sample with Fe-rich interface, we observe a dramatic decline in DMI value from 1.00 ± 0.18 mJ/m^2 to 0.15 ± 0.03 mJ/m^2, as shown in Table 2 (Details see Note S10 and Figure S17). Nearly an order of magnitude difference in the *D* values between two cases confirm that interfacial configurations have a significant impact on DMI, which is consistent with our theoretical calculations. In addition, current-induced hysteresis loop shift method[56] is also used to measure the DMI of Ta/Ir/CoFeB/MgO structures with $Co_{40}Fe_{40}B_{20}$ and $Co_{20}Fe_{60}B_{20}$ targets. The larger DMI value is found in the Fe-rich structure, which strongly supports our experiments and calculations above (For details see Note S11 and Figure S18).

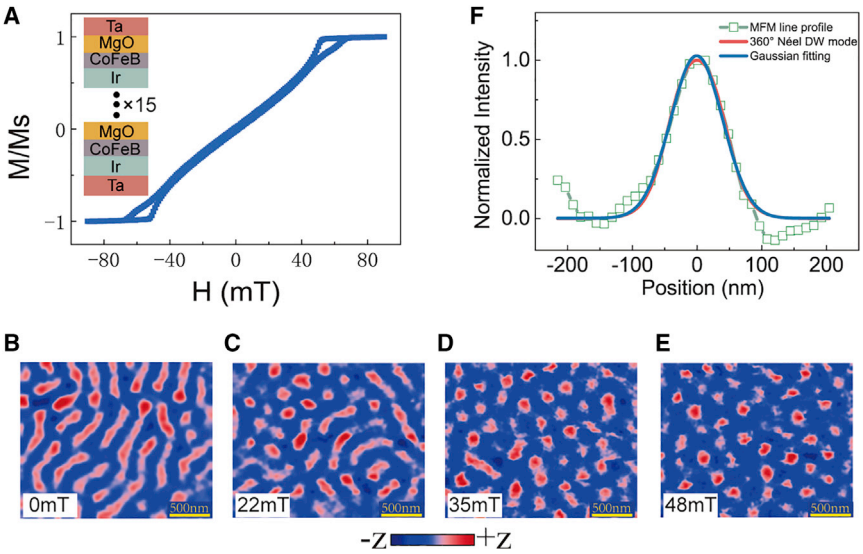

Figure 6. Room-temperature observation of isolated skyrmions

(A) The hysteresis loops with out-of-plane (OP) field for the multilayer stack shown in the inset.

(B–E) MFM images with scale bar of 500 nm, by detecting phase offsets, taken under different external magnetic field, (B) for $\mu_0 H_{ext}$ = 0 mT, (C) for $\mu_0 H_{ext}$ = 22 mT, (D) for $\mu_0 H_{ext}$ = 35 mT, and (E) for $\mu_0 H_{ext}$ = 48 mT. The images share the same color scale below (C) and (D), indicating the normalized z-component magnetization. The magnetic configuration transforms gradually from a mixed domain state under lower magnetic field, to isolated skyrmions state.

(F) The normalized line profile extracted from MFM image of one skyrmion, and the simulative profile using the 360° Néel domain wall model (More profiles can be seen in Note S12 and Figure S21). The solid blue line is the corresponding fittings of Gauss peak function, from where we can obtain the skyrmions diameter using the full width at half maximum (FWHM)) of the peak.

Overall, the large DMI we have achieved mainly originates from two parts: the good quality of Ir/CoFeB interface induced by Ta buffer layer could contribute to a larger DMI than the disordered interfaces,[57] which has been confirmed by our experiments and other reports;[36,58,59] on the other hand, the Ir/CoFeB structure with Fe-rich interface leads to more bonding of Ir and Fe elements at the interface, resulting in a higher DMI.

Experimental observation of sub-100

Based on the large DMI in Ir/CoFeB system, which is significantly larger than the threshold required to stabilize chiral Néel domain walls with $D_c = 2ln(2)\mu_0 Ms^2 t/\pi$, it is possible to generate chiral skyrmions under some external stimulations in such system, like current pulse or magnetic field.[20,60] We use MFM to image the nucleation of skyrmions. To increase the effective magnetic volume and demagnetization field, we engineer multilayer stacks composed of multiple repetitions of Ir/CoFeB/MgO structure.[61] Sample of Sub/Ta/[Ir/$Co_{20}Fe_{60}B_{20}$(1.1nm)/MgO]$_{15}$/Ta shown in the inset of Figure 6A is grown using sputtering system, and Figure 6A shows the magnetic hysteresis loops, which exhibit a typical sheared shape. The HR-TEM measurement was also applied to see the quality of the multilayer, it can be seen that as in the Ir/CoFeB/MgO film, the multilayer film also has higher film quality (See Note S5 for more details).

In Figures 6B–6E, the evolution of magnetic domain configuration under increasing out-of-plane fields is depicted with a field of view of 2.5 μm × 2 μm. The magnetic structure in this multilayer is determined by the competition between DM interaction, dipole-dipole interaction, magnetic anisotropy, and exchange interaction,

where a strong DMI will help to impose a certain chirality to the spin texture and improve the stability of skyrmions.[62] The strengthened dipole-dipole interaction in the periodically repeated Ir/CoFeB/MgO structure leads to the appearance of labyrinth domain at zero field. With the increase of magnetic fields, the labyrinthine domains tend to be broken into stripe domains, then gradually shrink and transform into isolated skyrmions, and finally reach the saturated magnetization state at 67 mT. It is worth mentioning that skyrmions can be created in a large range of magnetic fields from 22 mT to 58 mT, especially taking into account the large DMI value induced at the Ir/CoFeB interface.[63] A recent report explored that Ta/CoFeB/MgO stacks with smaller DMI compared with Pt (W)/CoFeB/MgO will prevent skyrmions from being stabilized in magnetic fields.[64] (More MFM images are displayed in Note S12 and Figures S19 and S20). As captured in Figures 6D and 6E, we can see isolated skyrmions states that remain almost unchanged under different magnetic field. Here, this stability of isolated skyrmions against annihilation into the ferromagnetic background under magnetic field can be attributed to DMI as well.[65] In Figure 6F, we provide the line sections extracted form MFM phase signals for several skyrmions (Indicated in Note S12 and Figure S21). The contrast of line profile varies continuously from the core to the side, without any side peaks or plateau in the center,[66] which matches sufficiently well with the simulative fitting using a chiral skyrmion and a 360° Néel domain wall model[67,68] (Details about the simulation can be found in Note S12). This good agreement of the out-of-plane profiles helps to demonstrate that what we observe are skyrmions rather than magnetic bubbles. Meanwhile, the fitting of Gauss peak function is applied to the profile to estimate the skyrmion diameter, defined as the full width at half maximum (FWHM) of the peak. The average skyrmion size is calculated to be 104.62 nm $\pm$ 15.05 nm, which consists well with the skyrmion diameter 104.86 nm $\pm$ 15.77 nm extracted from the 360°domain wall model fitting. It indicates that we see skyrmions ranging down to sub-100-nm dimensions that are stable at room temperature and can be realized in the successively coupled Ir/CoFeB/MgO multilayers.

The visible skyrmions stabilized at room temperature in Ir/CoFeB/MgO multilayers make this structure promising toward the proposals of skyrmion-based devices—for example, racetrack memory,[7,14] logic gates,[69] and artificial neuromorphic devices with high performance.[70–73] Besides, as Ir/CoFeB/MgO is an important constituent part of MTJs, by altering DMI, anisotropy, and other magnetic proprieties, it is possible to realize the electrical detection of skyrmions through various magnetoresistive effects like TMR.

In summary, we demonstrate that Ir/CoFeB/MgO structures exhibit a large DMI, which is revealed in a combined detailed investigation of first-principles calculations and BLS experiments. We attribute the significantly strong DMI to the good quality, and more importantly, the Fe-rich state of the interface between Ir and CoFeB layers. Furthermore, sub-100-nm magnetic skyrmions at room temperature are observed in this system. The discovery of the large DMI in Ir/CoFeB/MgO structures, combined with the evidence of room-temperature skyrmions, may provide a superior materials platform to realize skyrmionics, especially the nucleation and electrical detection of skyrmions in p-MTJs. Our work put forth pathways for the systematic engineering of skyrmion-based systems.

EXPERIMENTAL PROCEDURES

Resource availability

Lead contact

Further information and requests for resources should be directed to and will be fulfilled by the lead contact, Weisheng Zhao, weisheng.zhao@buaa.edu.cn.

Materials availability

This study did not generate new unique reagents.

Data and code availability

The authors declare that the data supporting the findings of this study are available within the article and the supplemental information. All other data are available from the lead contact upon reasonable request

First principles calculations

In order to calculate the DMI, we performed constrained spin-spiral supercell method calculations using the Vienna *ab initio* simulation package (VASP) code based on the generalized gradient approximation (GGA) of the Perdew-Burke-Ernzerhof (PBE) form and the projector augmented wave (PAW) method.[74–76] We used a kinetic-energy cutoff of 500 eV and a Γ-centered Monkhorst-Pack k-point mesh of 6 × 24 × 1 for all the calculations, which were verified to be sufficient to ensure a good convergence of the DMI. The energy convergence criteria of all the calculations were set as 1.0×10^{-7} eV and the structures were fully relaxed until the forces on the atoms became smaller than 0.001 eV/Å. The total microscopic DMI strength d^{tot} per bond can be introduced according to $d^{tot} = (E_{CW} - E_{CCW})/8$ with E_{CW} and E_{CCW} representing the clockwise (CW) energy and the counterclockwise (CCW) energy for opposite chirality spin textures respectively. The DMI strength can also be expressed by the micromagnetic energy per volume unit of the magnetic film with the corresponding coefficient $D^{tot} = \frac{2d^{tot}}{N_F r^2}$, in which r is the distance between two nearest neighbor magnetic atoms and N_F is the number of magnetic layers.[28]

The total microscopic DMI energy can be resolved by contributions from each magnetic layer according to $\triangle E_{DMI}^{tot} = \triangle E_{DMI}^{Co1} + \triangle E_{DMI}^{Fe2} + \triangle E_{DMI}^{Co3} + \triangle E_{DMI}^{Fe4} + \triangle E_{DMI}^{Co5} = \triangle E_{Intra} + \triangle E_{Inter} = 8(d^{Co1} + d^{Fe2} + d^{Co3} + d^{Fe4} + d^{Co5}) + 8\sqrt{2}(d^{Co1Fe2} + d^{Fe2Co3} + d^{Co3Fe4} + d^{Fe4Co5})$, where $\triangle E_{Intra}$ and $\triangle E_{Inter}$ are intralayer contributions and interlayer contributions, respectively (Co-terminated structure for example). This approach allows extracting layer-resolved DMI strength d^k, which contains the intralayer contributions of DMI (d^{Co1}, d^{Fe2}, d^{Co3}, d^{Fe4}, d^{Co5}) and the interlayer contributions of DMI (d^{Co1Fe2}, d^{Fe2Co3}, d^{Co3Fe4}, d^{Fe4Co5}).[28] For brevity, we replace d^{Co1Fe2}, d^{Fe2Co3}, d^{Co3Fe4}, d^{Fe4Co5} with d^{L12}, d^{L23}, d^{L34}, d^{L45}, respectively. The layer-resolved SOC energy distributions can be expressed by $\triangle E_{SOC}^{k,k'}$, where k is the magnetic layer corresponds to the layer-resolved DMI strength d^k and k' is the atomic layer that corresponds to the SOC energy difference. One can change the spin configuration of opposite chiralities in magnetic layer k and then directly extract the SOC energy difference of atomic layer k' from constrained spin-spiral supercell method calculations. The SOC energy source of interfacial Ir atoms ($\triangle E_{SOC}^{Fe1,Ir1}$ for Fe-terminated case and $\triangle E_{SOC}^{Co1\&Fe2,Ir1}$ for Co-terminated case) can be further decomposed into the contributions from each 5d orbital of interfacial Ir atoms. This 5*d* orbital-resolved SOC energy of interfacial Ir atoms can be extracted from the results of spin-spiral calculations.

In the DMI calculations, our asymmetric X/CoFe films consist of three X monolayers, five CoFe monolayers, and a 15 Å vacuum layer. The body-centered cubic structure was adopted for the CoFe (001). To minimize the lattice mismatch, a face-centered cubic structure was used for the X (001), with X [110] direction parallel to the CoFe [100] direction. The hollow structures with Fe-terminated and Co-terminated configurations at the X/CoFe interface were utilized since the hollow structure is the most energetically favorable.[77]

Sample preparation

The magnetic films were prepared at room temperature in an AJA International (ATC ORION 8) Physical Vapor deposited on a thermally oxidized Si wafer (on an area of 3 cm × 3 cm) by DC and RF Deposition System with the ultimate vacuum of 2×10^{-8} Torr and without applying magnetic fields. The Ta layer was deposited using DC power supply; other materials were deposited using RF power supply. The deposition rates were 1 nm/min for Ta at Ar pressure of 2 mTorr, 0.18 nm/min for MgO at Ar pressure of 0.6 mTorr, 0.33 nm/min for $Co_{20}Fe_{60}B_{20}$ at Ar pressures of 0.6 mTorr, and 0.88 nm/min for Ir at Ar pressures of 2 mTorr. During deposition, the sample rotates at a rate of about 7–8 cycles per minute. The top Ta layer prevents the film from air-passivation. The bottom Ta was grown as a buffer layer to provide better interface uniformity and film crystallization. An alloy target with the composition of $Co_{20}Fe_{60}B_{20}$ (in atomic percent) was used to deposit the CoFeB layer. The ratio of Co to Fe in the deposited CoFeB layer was also close to the ratio of the target material (See Note S4 and Figure S7 for more details). The MgO target was used to deposit the MgO layer.

All the samples are annealed in vacuum (better than 5×10^{-6} Torr) at different temperatures (175°C, 200°C, and 250°C) under an out-of-plane field of 1 T using the high vacuum annealing furnace. The set temperature rise time is half an hour, the holding time is half an hour, and then the temperature drops naturally.

Sample characterization

The *M-H* curve was obtained by a LakeShore 8600 series vibrating sample magnetometer (VSM) equipment. The magnetic field direction of the equipment is fixed, and the *M-H* curve under the out-of-plane magnetic field and in-plane magnetic field is measured by rotating the sample. The size of the samples in the VSM test is about 1 cm × 0.5 cm. A vernier caliper and ImageJ software were used to measure the area of the sample. By obtaining the moment *M* in the hysteresis loop and measuring the area of the sample, the saturated magnetic moment M_s of the sample can be obtained by linear fitting.

The sample for transmission electron microscopy was prepared by the Helios G4-UX FIB equipment. The HR-TEM analysis was obtained by the Talos F200X HR-TEM equipment.

Brillouin light-scattering

BLS measurements were performed to study frequency shift of the counterpropagating Damon-Eshbach spin waves induced by DMI. The details of BLS setup to realize Damon–Eshbach (DE) geometry can be found in the inset of Figure 3A, where a single mode diode pump solid-state laser (wavelength of 532 nm and power of 200 mW) is used, and an external in-plane field is applied. We used a six-pass Fabry-Perot interferometer to analyze the back-scattered light collected. The spectra were obtained through the accumulation of photons after several hours; it ensures the accuracy of fitted Stokes (Anti-Stokes) peak values. We chose a free spectral range of (FSR) 40 GHz and a 2^9 multi-channel analyzer. The frequency resolution estimated by FSR/2^9 is less than 0.1 GHz.

Magnetic force microscopy

We performed MFM measurements at room temperature, using the Bruker Dimension Icon Atomic Force Microscope (AFM) system. Samples were placed over a custom electromagnet where the external perpendicular magnetic field can be applied. Commercial magnetic probes with low magnetic moment (Nanosensors

PPP-MFMR-LM) were chosen to minimize the tip perturbations on magnetic configurations of samples. The nominal cantilever spring constant, frequency, and scan rate were 2.8 k/N, 75 kHz and 0.7 Hz, respectively. To confirm the evolution of magnetic domains, we scanned different areas with different scan sizes. They exhibit similar trends with external magnetic field (See Note S12 and Figures S19 and S20).

SUPPLEMENTAL INFORMATION

Supplemental information can be found online at https://doi.org/10.1016/j.xcrp.2021.100618.

ACKNOWLEDGMENTS

The authors would like to thank the supports by the projects from National Natural Science Foundation of China (No.61627813, 61571023, and 62004013), the National Key Technology Program of China 2017ZX01032101, the Program of Introducing Talents of Discipline to Universities in China, China, (No. B16001), the Beihang Hefei Innovation Research Institute Project BHKX-19-02, and Beijing Municipal Science and Technology Project under Grant Z201100004220002.

AUTHOR CONTRIBUTIONS

W.Z. initialized, conceived, and supervised the project. R.C., X.W., H.C. contributed equally to this work. R.C. performed the first-principles calculations under supervision of S.P., and H.Y. helped analyze the results. H.C. and D.X. performed sample fabrication, magnetic characterization, and magnetic properties analysis. X.W., D.X., S.L., and X.Z. conducted BLS measurements and spectra analysis. K.L., J.K., and M.K. conducted the current-induced hysteresis loop shift measurements. X.W. and H.Z. performed MFM measurements, and S.L. and K.C. helped analyze the images. R.C., X.W., and H.C. wrote the manuscript. All the authors participated in the discussion and the interpretation of the various results.

DECLARATION OF INTERESTS

The authors declare no competing interests.

Received: June 7, 2021
Revised: August 22, 2021
Accepted: September 30, 2021
Published: October 27, 2021

REFERENCES

1. Dzyaloshinsky, I. (1958). A thermodynamic theory of "weak" ferromagnetism of antiferromagnetics. J. Phys. Chem. Solids *4*, 241.

2. Moriya, T. (1960). Anisotropic superexchange interaction and weak ferromagnetism. Phys. Rev. *120*, 91.

3. Fert, A., and Levy, P.M. (1980). Role of anisotropic exchange interactions in determining the propertiesof spin-glasses. Phys. Rev. Lett. *44*, 1538.

4. Robertson, M., Agostino, C.J., Chen, G., Kang, S.P., Mascaraque, A., Michel, E.G., Won, C., Wu, Y., Schmid, A.K., and Liu, K. (2020). In-plane Néel wall chirality and orientation of interfacial Dzyaloshinskii-Moriya vector in magnetic films. Phys. Rev. B *102*, 024417.

5. Jiang, W., Chen, G., Liu, K., Zang, J., Velthuis, S.G.E., and Hoffmann, A. (2017). Skyrmions in magnetic multilayers. Phys. Rep. *704*, 1–49.

6. Jiang, W., Upadhyaya, P., Zhang, W., Yu, G., Jungfleisch, M.B., Fradin, F.Y., Pearson, J.E., Tserkovnyak, Y., Wang, K.L., Heinonen, O., et al. (2015). Magnetism. Blowing magnetic skyrmion bubbles. Science *349*, 283–286.

7. Guan, Y., Zhou, X., Ma, T., Bläsing, R., Deniz, H., Yang, S.H., and Parkin, S.S.P. (2021). Increased efficiency of current-induced motion of chiral domain walls by interface engineering. Adv. Mater. *33*, e2007991.

8. Jiang, W., Zhang, X., Yu, G., Zhang, W., Wang, X., Jungfleisch, M.B., Pearson, J.E., Cheng, X., Heinonen, O., Wang, K.L., et al. (2017). Direct observation of the skyrmion Hall effect. Nat. Phys. *13*, 162–169.

9. Fert, A.R. (1991). Magnetic and transport properties of metallic multilayers. Mater. Sci. Forum *59–60*, 439–480..

10. Cho, J., Kim, N.-H., Lee, S., Kim, J.-S., Lavrijsen, R., Solignac, A., Yin, Y., Han, D.-S., van Hoof, N.J., Swagten, H.J.M., et al. (2015). Thickness dependence of the interfacial Dzyaloshinskii-Moriya interaction in inversion symmetry broken systems. Nat. Commun. *6*, 7635.

11. Wang, L., Liu, C., Mehmood, N., Han, G., Wang, Y., Xu, X., Feng, C., Hou, Z., Peng, Y., Gao, X., and Yu, G. (2019). Construction of a room-temperature Pt/Co/Ta multilayer film with ultrahigh-density skyrmions for memory

application. ACS Appl. Mater. Interfaces *11*, 12098–12104.

12. Moreau-Luchaire, C., Mouta S, C., Reyren, N., Sampaio, J., Vaz, C.A.F., Van Horne, N., Bouzehouane, K., Garcia, K., Deranlot, C., Warnicke, P., et al. (2016). Additive interfacial chiral interaction in multilayers for stabilization of small individual skyrmions at room temperature. Nat. Nanotechnol. *11*, 444–448.

13. Boulle, O., Vogel, J., Yang, H., Pizzini, S., de Souza Chaves, D., Locatelli, A., Menteş, T.O., Sala, A., Buda-Prejbeanu, L.D., Klein, O., et al. (2016). Room-temperature chiral magnetic skyrmions in ultrathin magnetic nanostructures. Nat. Nanotechnol. *11*, 449–454.

14. Amara, S., Sevilla, G.A.T., Hawsawi, M., Mashraei, Y., Mohammed, H., Cruz, M.E., Ivanov, Y.P., Jaiswal, S., Jakob, G., Kläui, M., et al. (2018). High-performance flexible magnetic tunnel junctions for smart miniaturized instruments. Adv. Eng. Mater. *20*, 1800471.

15. Crum, D.M., Bouhassoune, M., Bouaziz, J., Schweflinghaus, B., Blügel, S., and Lounis, S. (2015). Perpendicular reading of single confined magnetic skyrmions. Nat. Commun. *6*, 8541.

16. Hanneken, C., Otte, F., Kubetzka, A., Dupé, B., Romming, N., von Bergmann, K., Wiesendanger, R., and Heinze, S. (2015). Electrical detection of magnetic skyrmions by tunnelling non-collinear magnetoresistance. Nat. Nanotechnol. *10*, 1039–1042.

17. Guo, Z., Yin, J., Bai, Y., Zhu, D., Shi, K., Wang, G., Cao, K., and Zhao, W. (2021). Spintronics for energy- efficient computing: An overview and outlook. Proc. IEEE *109*, 1398–1417.

18. Cheng, H., Chen, J., Peng, S., Zhang, B., Wang, Z., Zhu, D., Shi, K., Eimer, S., Wang, X., Guo, Z., et al. (2020). Giant perpendicular magnetic anisotropy in mo-based double-interface free layer structure for advanced magnetic tunnel junctions. Adv. Electron. Mater. *6*, 2000271.

19. Zhou, J., Zhou, H., Bournel, A., and Zhao, W. (2020). Large spin Hall effect and tunneling magnetoresistance in iridium-based magnetic tunnel junctions. Sci. China Phys. Mech. Astron. *63*, 217511.

20. Woo, S., Litzius, K., Krüger, B., Im, M.Y., Caretta, L., Richter, K., Mann, M., Krone, A., Reeve, R.M., Weigand, M., et al. (2016). Observation of room-temperature magnetic skyrmions and their current-driven dynamics in ultrathin metallic ferromagnets. Nat. Mater. *15*, 501–506.

21. Zhang, X., Cai, W., Zhang, X., Wang, Z., Li, Z., Zhang, Y., Cao, K., Lei, N., Kang, W., Zhang, Y., et al. (2018). Skyrmions in magnetic tunnel junctions. ACS Appl. Mater. Interfaces *10*, 16887–16892.

22. Penthorn, N.E., Hao, X., Wang, Z., Huai, Y., and Jiang, H.W. (2019). Experimental observation of single skyrmion signatures in a magnetic tunnel junction. Phys. Rev. Lett. *122*, 257201.

23. Cho, S., Baek, S.C., Lee, K.D., Jo, Y., and Park, B.G. (2015). Large spin Hall magnetoresistance and its correlation to the spin-orbit torque in W/CoFeB/MgO structures. Sci. Rep. *5*, 14668.

24. Ikeda, S., Miura, K., Yamamoto, H., Mizunuma, K., Gan, H.D., Endo, M., Kanai, S., Hayakawa, J., Matsukura, F., and Ohno, H. (2010). A perpendicular-anisotropy CoFeB-MgO magnetic tunnel junction. Nat. Mater. *9*, 721–724.

25. Zhu, L., Ralph, D.C., and Burhman, R.A. (2021). Maximizing spin-orbit torque generated by the spin Hall effect of Pt. Appl. Phys. Rev. *8*, 031308.

26. Ma, X., Yu, G., Tang, C., Li, X., He, C., Shi, J., Wang, K.L., and Li, X. (2018). Interfacial Dzyaloshinskii-Moriya interaction: Effect of 5d band filling and correlation with spin mixing conductance. Phys. Rev. Lett. *120*, 157204.

27. Ma, X., Yu, G., Li, X., Wang, T., Wu, D., Olsson, K.S., Chu, Z., An, K., Xiao, J.Q., Wang, K.L., et al. (2016). Interfacial control of Dzyaloshinskii-Moriya interaction in heavy metal/ferromagnetic metal thin film heterostructures. Phys. Rev. B *94*, 180408.

28. Yang, H., Thiaville, A., Rohart, S., Fert, A., and Chshiev, M. (2015). Anatomy of Dzyaloshinskii-Moriya interaction at Co/Pt interfaces. Phys. Rev. Lett. *115*, 267210.

29. Yang, H., Chen, G., Cotta, A.A.C., N'Diaye, A.T., Nikolaev, S.A., Soares, E.A., Macedo, W.A.A., Liu, K., Schmid, A.K., Fert, A., and Chshiev, M. (2018). Significant Dzyaloshinskii-Moriya interaction at graphene-ferromagnet interfaces due to the Rashba effect. Nat. Mater. *17*, 605–609.

30. Belabbes, A., Bihlmayer, G., Bechstedt, F., Blügel, S., and Manchon, A. (2016). Hund's rule-driven Dzyaloshinskii-Moriya interaction at 3d-5d interfaces. Phys. Rev. Lett. *117*, 247202.

31. Kashid, V., Schena, T., Zimmermann, B., Mokrousov, Y., Blügel, S., Shah, V., and Salunke, H.G. (2014). Dzyaloshinskii-Moriya interaction and chiral magnetism in 3d-5d zigzag chains: Tight-binding model and *ab initio* calculations. Phys. Rev. B Condens. Matter Mater. Phys. *90*, 054412.

32. Jadaun, P., Register, L.F., and Banerjee, S.K. (2020). The microscopic origin of DMI in magnetic bilayers and prediction of giant DMI in new bilayers. npj. Comp. Mater. *6*, 88.

33. Yang, B., Cui, Q., Liang, J., Chshiev, M., and Yang, H. (2020). Reversible control of Dzyaloshinskii-Moriya interaction at the graphene/Co interface via hydrogen absorption. Phys. Rev. B *101*, 014406.

34. Lin, W., Yang, B., Chen, A.P., Wu, X., Guo, R., Chen, S., Liu, L., Xie, Q., Shu, X., Hui, Y., et al. (2020). Perpendicular magnetic anisotropy and Dzyaloshinskii-Moriya interaction at an oxide/ferromagnetic metal interface. Phys. Rev. Lett. *124*, 217202.

35. Heide, M., Bihlmayer, G., and Blügel, S. (2009). Describing Dzyaloshinskii–Moriya spirals from first principles. Phys. B. Condens. Matter *404*, 2678–2683.

36. Conte, R.L., Martinez, E., Hrabec, A., Lamperti, A., Schulz, T., Nasi, L., et al. (2015). Role of B diffusion in the interfacial Dzyaloshinskii-Moriya interaction in Ta/$Co_{20}Fe_{60}B_{20}$/MgO nanowires. Phys. Rev. B Condens. Matter Mater. Phys. *91*, 014433.

37. Moon, J.-H., Seo, S.-M., Lee, K.-J., Kim, K.-W., Ryu, J., Lee, H.-W., McMichael, R.D., and Stiles, M.D. (2013). Spin-wave propagation in the presence of interfacial Dzyaloshinskii-Moriya interaction. Phys. Rev. B. *88*, 184404.

38. Di, K., Zhang, V.L., Lim, H.S., Ng, S.C., Kuok, M.H., Yu, J., Yoon, J., Qiu, X., and Yang, H. (2015). Direct observation of the Dzyaloshinskii-Moriya interaction in a Pt/Co/Ni film. Phys. Rev. Lett. *114*, 047201.

39. Nembach, H.T., Shaw, J.M., Weiler, M., Jué, E., and Silva, T.J. (2015). Linear relation between Heisenberg exchange and interfacial Dzyaloshinskii–Moriya interaction in metal films. Nat. Phys. *11*, 825–829.

40. Ma, X., Yu, G., Razavi, S.A., Sasaki, S.S., Li, X., Hao, K., Tolbert, S.H., Wang, K.L., and Li, X. (2017). Dzyaloshinskii-Moriya interaction across an antiferromagnet-ferromagnet interface. Phys. Rev. Lett. *119*, 027202.

41. Kim, G.W., Samardak, A.S., Kim, Y.J., Cha, I.H., Ognev, A.V., Sadovnikov, A.V., Nikitov, S.A., and Kim, Y.K. (2018). Role of the heavy metal's crystal phase in oscillations of perpendicular magnetic anisotropy and the interfacial Dzyaloshinskii-Moriya interaction in W/Co-Fe-B/MgO films. Phys. Rev. Appl. *9*, 064005.

42. Skowroński, W., Nozaki, T., Shiota, Y., Tamaru, S., Yakushiji, K., Kubota, H., Fukushima, A., Yuasa, S., and Suzuki, Y. (2015). Perpendicular magnetic anisotropy of Ir/CoFeB/MgO trilayer system tuned by electric fields. Appl. Phys. Express *8*, 053003.

43. Chaurasiya, A.K., Choudhury, S., Sinha, J., and Barman, A. (2018). Dependence of interfacial Dzyaloshinskii-Moriya interaction on layer thicknesses in Ta/CoFeB/TaO_x heterostructures from Brillouin light scattering. Phys. Rev. Appl. *9*, 014008.

44. Srivastava, T., Schott, M., Juge, R., Křižáková, V., Belmeguenai, M., Roussigné, Y., Bernand-Mantel, A., Ranno, L., Pizzini, S., Chérif, S.-M., et al. (2018). Large-voltage tuning of Dzyaloshinskii-Moriya interactions: A route toward dynamic control of skyrmion chirality. Nano Lett. *18*, 4871–4877.

45. Soucaille, R., Belmeguenai, M., Torrejon, J., Kim, J.-V., Devolder, T., Roussigné, Y., Chérif, S.-M., Stashkevich, A.A., Hayashi, M., and Adam, J.-P. (2016). Probing the Dzyaloshinskii-Moriya interaction in CoFeB ultrathin films using domain wall creep and Brillouin light spectroscopy. Phys. Rev. B *94*, 104431.

46. Chaurasiya, A.K., Banerjee, C., Pan, S., Sahoo, S., Choudhury, S., Sinha, J., and Barman, A. (2016). Direct observation of interfacial Dzyaloshinskii-Moriya interaction from asymmetric spin-wave propagation in W/CoFeB/SiO_2 heterostructures down to sub-nanometer CoFeB Thickness. Sci. Rep. *6*, 32592.

47. Tacchi, S., Troncoso, R.E., Ahlberg, M., Gubbiotti, G., Madami, M., Åkerman, J., and Landeros, P. (2017). Interfacial Dzyaloshinskii-Moriya interaction in Pt/CoFeB films: Effect of the heavy-metal thickness. Phys. Rev. Lett. *118*, 147201.

48. Di, K., Zhang, V.L., Lim, H.S., Ng, S.C., Kuok, M.H., Qiu, X., and Yang, H. (2015). Asymmetric spin-wave dispersion due to Dzyaloshinskii-Moriya interaction in an ultrathin Pt/CoFeB film. Appl. Phys. Lett. *106*, 052403.

49. Chen, Y., Zhang, Q., Jia, J., Zheng, Y., Wang, Y., Fan, X., and Cao, J. (2018). Tuning Slonczewski-like torque and Dzyaloshinskii–Moriya interaction by inserting a Pt spacer layer in Ta/CoFeB/MgO structures. Appl. Phys. Lett. *112*, 232402.

50. Cho, J., Kim, N.-H., Jung, J., Han, D.-S., Swagten, H.J.M., Kim, J.-S., and You, C.-Y. (2018). Thermal Annealing Effects on the Interfacial Dzyaloshinskii–Moriya Interaction Energy Density and Perpendicular Magnetic Anisotropy. IEEE Trans. Magn. *54*, 1500104.

51. Cho, J., Kim, N.-H., Kang, S.K., Hwang, H.-K., Jung, J., Swagten, H.J.M., Kim, J.-S., and You, C.-Y. (2017). The sign of the interfacial Dzyaloshinskii–Moriya interaction in ultrathin amorphous and polycrystalline magnetic films. J. Phys. D Appl. Phys. *50*, 425004.

52. Belmeguenai, M., Bouloussa, H., Roussigné, Y., Gabor, M.S., Petrisor, T., Tiusan, C., Yang, H., Stashkevich, A., and Chérif, S.M. (2017). Interface Dzyaloshinskii-Moriya interaction in the interlayer antiferromagnetic-exchange coupled Pt/CoFeB/Ru/CoFeB systems. Phys. Rev. B *96*, 144402.

53. Wang, X., Cao, A., Li, S., Tang, J., Du, A., Cheng, H., et al. (2021). Manipulating density of magnetic skyrmions via multilayer repetition and thermal annealing. Phys. Rev. B *104*, 064421.

54. Watanabe, K., Fukami, S., Sato, H., Ikeda, S., Matsukura, F., and Ohno, H. (2017). Annealing temperature dependence of magnetic properties of CoFeB/MgO stacks on different buffer layers. Jpn. J. Appl. Phys *56*, 0802B2.

55. Almasi, H., Xu, M., Xu, Y., Newhouse-Illige, T., and Wang, W.G. (2016). Effect of Mo insertion layers on the magnetoresistance and perpendicular magnetic anisotropy in Ta/CoFeB/MgO junctions. Appl. Phys. Lett. *109*, 032401.

56. Pai, C., Mann, M., Tan, A.J., and Beach, G.S.D. (2016). Determination of spin torque efficiencies in heterostructures with perpendicular magnetic anisotropy. Phys. Rev. B *93*, 144409.

57. Zimmermann, B., Legrand, W., Maccariello, D., Reyren, N., Cros, V., Blügel, S., and Fert, A. (2018). Dzyaloshinskii-Moriya interaction at disordered interfaces from *ab initio* theory: Robustness against intermixing and tunability through dusting. Appl. Phys. Lett. *113*, 232403.

58. Kim, N.-H., Han, D.-S., Jung, J., Cho, J., Kim, J.-S., Swagten, H.J.M., and You, C.-Y. (2015). Improvement of the interfacial Dzyaloshinskii-Moriya interaction by introducing a Ta buffer layer. Appl. Phys. Lett. *107*, 142408.

59. Wells, A.W.J., Shepley, P.M., Marrows, C.H., and Moore, T.A. (2017). Effect of interfacial intermixing on the Dzyaloshinskii-Moriya interaction in Pt/Co/Pt. Phys. Rev. B *95*, 054428.

60. Jaiswal, S., Litzius, K., Lemesh, I., Büttner, F., Finizio, S., Raabe, J., Weigand, M., Lee, K., Langer, J., Ocker, B., et al. (2017). Investigation of the Dzyaloshinskii-Moriya interaction and room temperature skyrmions in W/CoFeB/MgO thin films and microwires. Appl. Phys. Lett. *111*, 022409.

61. Back, C., Cros, V., Ebert, H., Everschor-Sitte, K., Fert, A., Garst, M., Ma, T., Mankovsky, S., Monchesky, T.L., Mostovoy, M., et al. (2020). The 2020 skyrmionics roadmap. J. Phys. D Appl. Phys. *53*, 363001.

62. Soumyanarayanan, A., Raju, M., Gonzalez Oyarce, A.L., Tan, A.K.C., Im, M.-Y., Petrović, A.P., Ho, P., Khoo, K.H., Tran, M., Gan, C.K., et al. (2017). Tunable room-temperature magnetic skyrmions in Ir/Fe/Co/Pt multilayers. Nat. Mater. *16*, 898–904.

63. Büttner, F., Lemesh, I., and Beach, G.S.D. (2018). Theory of isolated magnetic skyrmions: From fundamentals to room temperature applications. Sci. Rep. *8*, 4464.

64. Casiraghi, A., Corte-León, H., Vafaee, M., Garcia-Sanchez, F., Durin, G., Pasquale, M., Jakob, G., Kläui, M., and Kazakova, O. (2019). Individual skyrmion manipulation by local magnetic field gradients. Commun. Phys. *2*, 145.

65. Bogdanov, A., and Hubert, A. (1994). Thermodynamically stable magnetic vortex states in magnetic crystals. J. Magn. Magn. Mater. *138*, 255–269.

66. Bhattacharya, D., Razavi, S.A., Wu, H., Dai, B., Wang, K.L., and Atulasimha, J. (2020). Creation and annihilation of non-volatile fixed magnetic skyrmions using voltage control of magnetic anisotropy. Nat. Electron. *3*, 539–545.

67. Wang, X.S., Yuan, H.Y., and Wang, X.R. (2018). Magnetic skyrmion-based artificial neuron device. Commun. Phys. *1*, 31.

68. Romming, N., Kubetzka, A., Hanneken, C., von Bergmann, K., and Wiesendanger, R. (2015). Field-dependent size and shape of single magnetic Skyrmions. Phys. Rev. Lett. *114*, 177203.

69. Luo, S., Song, M., Li, X., Zhang, Y., Hong, J., Yang, X., Zou, X., Xu, N., and You, L. (2018). Reconfigurable skyrmion logic gates. Nano Lett. *18*, 1180–1184.

70. Li, S., Kang, W., Huang, Y., Zhang, X., Zhou, Y., and Zhao, W. (2017). Magnetic skyrmion-based artificial neuron device. Nanotechnology *28*, 31LT01.

71. Prychynenko, D., Sitte, M., Litzius, K., Krüger, B., Bourianoff, G., Kläui, M., Sinova, J., and Everschor-Sittel, K. (2018). Magnetic skyrmion as a nonlinear resistive element: A potential building block for reservoir computing. Phys. Rev. Appl. *9*, 014034.

72. Zázvorka, J., Jakobs, F., Heinze, D., Keil, N., Kromin, S., Jaiswal, S., Litzius, K., Jakob, G., Virnau, P., Pinna, D., et al. (2019). Thermal skyrmion diffusion used in a reshuffler device. Nat. Nanotechnol. *14*, 658–661.

73. Hong, J., Li, X., Xu, N., Chen, H., Cabrini, S., Khizroev, S., Bokor, J., and You, L. (2020). A dual magnetic tunnel junction-based neuromorphic device. Adv. Intell. Syst. *2*, 2000143.

74. Kresse, G., and Furthmüller, J. (1996). Efficient iterative schemes for *ab initio* total-energy calculations using a plane-wave basis set. Phys. Rev. B Condens. Matter *54*, 11169–11186.

75. Kresse, G., and Furthmüller, J. (1996). Efficiency of *ab initio* total energy calculations for metals and semiconductors using a plane-wave basis set. Comput. Mater. Sci. *6*, 15–50.

76. Kresse, G., and Hafner, J. (1993). *Ab initio* molecular dynamics for liquid metals. Phys. Rev. B Condens. Matter *47*, 558–561.

77. Peng, S., Wang, M., Yang, H., Zeng, L., Nan, J., Zhou, J., Zhang, Y., Hallal, A., Chshiev, M., Wang, K.L., et al. (2015). Origin of interfacial perpendicular magnetic anisotropy in MgO/CoFe/metallic capping layer structures. Sci. Rep. *5*, 18173.